# Radiative Heating Errors in Naturally Ventilated Air Temperature Measurements Made from Buoys*

STEVEN P. ANDERSON AND MARK F. BAUMGARTNER

*Department of Physical Oceanography, Woods Hole Oceanographic Institution, Woods Hole, Massachusetts*

(Manuscript received 23 April 1997, in final form 10 June 1997)

ABSTRACT

Solar radiative heating errors in buoy-mounted, naturally ventilated air temperature sensors are examined. Data from sensors with multiplate radiation shields and collocated, fan-aspirated air temperature sensors from three buoy deployments during TOGA COARE (Tropical Ocean Global Atmosphere Coupled Ocean–Atmosphere Response Experiment) and the Arabian Sea Mixed Layer Dynamics Experiment are used to describe the errors in the naturally ventilated measurements. The naturally ventilated sensors have mean daytime errors of 0.27°C and maximum instantaneous errors of 3.4°C. The errors are at times larger than the difference between the air and sea surface temperatures. These errors lead to mean daytime biases in sensible and latent heat fluxes of 1–4 W $m^{-2}$ and instantaneous errors up to 22 W $m^{-2}$. The heating errors increase with increasing shortwave radiation and diminish with increasing wind speed. The radiative heating is also found to be a function of sun elevation with maximum heating errors occurring at elevations of approximately 45°. A simple model of sensor heating that balances the radiative heating with convective and conductive cooling is presented. This model can be used with empirically determined coefficients and observations of wind speed and shortwave radiation to quantify the radiative heating errors in naturally ventilated air temperature sensors.

## 1. Introduction

The increased demand by climate research programs for accurate estimates of air–sea fluxes made from ships and buoys has led to an increased demand for accurate surface air temperature measurements. Radiative heating of the temperature sensor element is a significant source of error in these measurements. In general, radiative heating errors will increase with increasing solar radiation and decrease with increasing wind speed (Fig. 1). Ideally, a continuously aspirated temperature element would be used to reduce this error. However, the power required to drive a commercially available aspirator is currently too large to be practical for long-term (>1–2 month) remote deployments at sea. Instead, solar radiation shields are commonly used on buoys as the best available technology to minimize radiative heating errors in air temperature measurements. The approximately 70 buoys of the TAO array in the tropical Pacific (Hayes et al. 1991), 60 National Data Buoy Center (NDBC) buoys, and many of the 60 Coastal-Marine Automated Network (CMAN) stations in the coastal and continental shelf waters of the United States rely on naturally ventilated shielding to reduce radiative heating errors. With so many buoys in operation without fan-aspirated sensors, the problem of radiative heating must be acknowledged as a source of error in air temperature measurements and addressed.

The naturally ventilated, multiplate radiation shields commonly used for air temperature measurements on buoys were developed by Gill (1983). These shields were designed by Gill to meet specific performance criteria. The heating and cooling errors of the temperature element are not to exceed ± 1°, ±2°, and ±3°C at wind speeds above 5, 2, and 0.5 m $s^{-1}$, respectively. In addition, the shields will withstand 40 m $s^{-1}$ winds and wave breaking over the sensor without sustaining measurable damage. The design uses 12-cm-diameter ''pie plates'' made of white PVC. These plates are stackable and cover the sensor element completely, shading it from both direct radiative heating above and surface reflected radiation below.

The sensible heat flux at the ocean surface is roughly proportional to the difference between the air temperature and the sea surface skin temperature. This difference is often less than 2°C over the open ocean at low latitudes, as demonstrated by the observations presented here. Thus, a small error in air temperature measurements can lead to significant errors in the surface sensible heat flux estimates. The purpose of this study is to quantify the radiative heating error of naturally ven-

* WHOI Contribution Number 9482.

*Corresponding author address:* Dr. Steven P. Anderson, Department of Physical Oceanography, Woods Hole Oceanographic Institution, Mail Stop #29, Woods Hole, MA 02543.
E-mail: sanderson@whoi.edu.

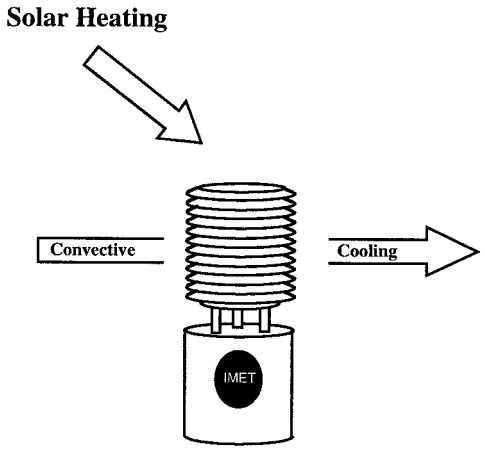


FIG. 1. The major heating and cooling processes affecting a naturally ventilated radiation shield.

tilated air temperature measurements made from buoys. Collocated aspirated temperature elements from three separate buoy deployments provide the reference to quantify observed errors. These data are used to derive a simple heat transfer model with empirically derived coefficients leading to an algorithm that quantifies the radiative heating errors. With this model, shortwave radiation and wind speed measurements from the buoy can be used to correct the observed air temperature measurements.

The role of the sensible heat flux term in the total energy budget at the sea surface is often quite small, sometimes an order of magnitude lower than the latent heat flux or net shortwave radiation. Consequently, improvements in the accuracy of measuring air–sea temperature differences may seem unnecessary since the contribution of the sensible heat flux is small. One of the objectives of the Tropical Ocean Global Atmosphere (TOGA) Coupled Ocean–Atmosphere Response Experiment (COARE) was to estimate the net heat flux to within 10 W $m^{-2}$ (Webster and Lukas 1992; Fairall et al. 1996a). By comparing estimates of sensible heat flux from fan-aspirated and naturally ventilated air temperature sensors, we observed instantaneous errors of up to 22.5 W $m^{-2}$. Recent studies of estimated sensible heat flux calculated from naturally ventilated sensors from TOGA COARE do not acknowledge potential biases due to radiative heating errors (Esbensen and McPhaden 1996; Lin and Johnson 1996). These errors must be addressed to estimate both the sensible and net heat flux to the desired accuracy.

Effective comparisons of in situ surface air temperatures with atmospheric model products are also compromised by radiative heating errors. Since daytime observations may be suspect, only nighttime measurements can be used to evaluate model products. This limits both the amount of data available for comparison and the ability to evaluate important diurnal processes. In addition to the problems of absolute accuracy, the shape of the diurnal cycle is altered in a predictable manner. At low latitudes, maximum heating of a multiplate shield does not occur at local solar noon, but at midmorning and midafternoon because of the shield geometry. This diurnal signal imposed by radiative heating errors can be misinterpreted as the manifestation of a boundary layer process. Users of naturally ventilated sensors aboard buoys need to be aware of the magnitude and the effects of radiative heating on air temperature measurements.

Section 2 is a review of the instrumentation used in this study and the field deployments. Section 3 presents the observations and quantifies radiative heating errors in the naturally ventilated air temperature sensors. A simple model of the radiative heating and a correction algorithm are described in section 4. Section 5 presents the results of applying the correction to the observations during the three deployments.

## 2. The instrumentation and deployments

The observations presented were taken from instruments mounted on three-meter discus buoys deployed in the tropical western Pacific and the Arabian Sea (Ta-

TABLE 1. Air temperature sensors deployed in the Arabian Sea Mixed Layer Experiment and TOGA COARE. Heights are reported relative to the sea surface.

| | Sensor | Ventilation | Data acquisition system | Height (m) | Collocated relative humidity | Sampling period |
|---|---|---|---|---|---|---|
| Arabian Sea | | | | | | |
| Aspirated | PRT | Aspiration | IMET | 2.2 | No | 1 min |
| IMET AT | PRT | Natural | IMET | 2.7 | No | 1 min |
| IMET RH | Thermistor | Natural | IMET | 2.7 | Yes | 1 min |
| VAWR | Thermistor | Natural | VAWR | 2.7 | No | 7.5 min |
| Stand-alone | Thermistor | Natural | Stand-alone | 3.0 | Yes | 3.75 min |
| TOGA COARE | | | | | | |
| Aspirated | PRT | Aspiration | IMET | 2.6 | No | 1 min |
| IMET AT | PRT | Natural | IMET | 2.6 | No | 1 min |
| IMET RH | Thermistor | Natural | IMET | 2.6 | Yes | 1 min |
| VAWR | Thermistor | Natural | VAWR | 2.7 | No | 7.5 min |

TABLE 2. Mean surface conditions during Arab 1, Arab 2, and TOGA COARE. Except for wind speed and shortwave radiation, the averaging interval includes only the times when the aspirator was turned on. Wind speed and shortwave radiation are averaged from deployment until the aspirator has depleted its batteries.

| | Arab 1 | Arab 2 | TOGA COARE |
|---|---|---|---|
| Aspiration duration (days) | 58.7 | 51.1 | 13.3 |
| Wind speed (m $s^{-1}$) | 5.78 | 4.69 | 4.28 |
| Shortwave radiation (W $m^{-2}$) | 233.8 | 305.5 | 198.4 |
| Air temperature (°C) | 26.93 | 29.00 | 28.16 |
| Daytime | 27.08 | 29.12 | 28.16 |
| Nighttime | 26.81 | 28.88 | — |
| Diurnal range | 0.52 | 0.80 | — |
| Sea surface temperature (°C) | 27.41 | 29.86 | 29.60 |
| Diurnal range | 0.22 | 0.66 | 0.40 |
| Skin temperature* (°C) | 27.17 | 29.60 | 29.55 |
| Diurnal range | 0.29 | 0.79 | 0.66 |
| Sensible heat flux (W $m^{-2}$) | −2.0 | −2.6 | −9.6 |
| Daytime | −1.3 | −2.7 | −9.6 |
| Nighttime | −2.7 | −2.5 | — |
| Latent heat flux (W $m^{-2}$) | −142.0 | −113.7 | −120.7 |
| Daytime | −143.6 | −120.2 | −120.7 |
| Nighttime | −140.8 | −106.8 | — |

* Estimated using the parameterization of Fairall et al. (1996b).

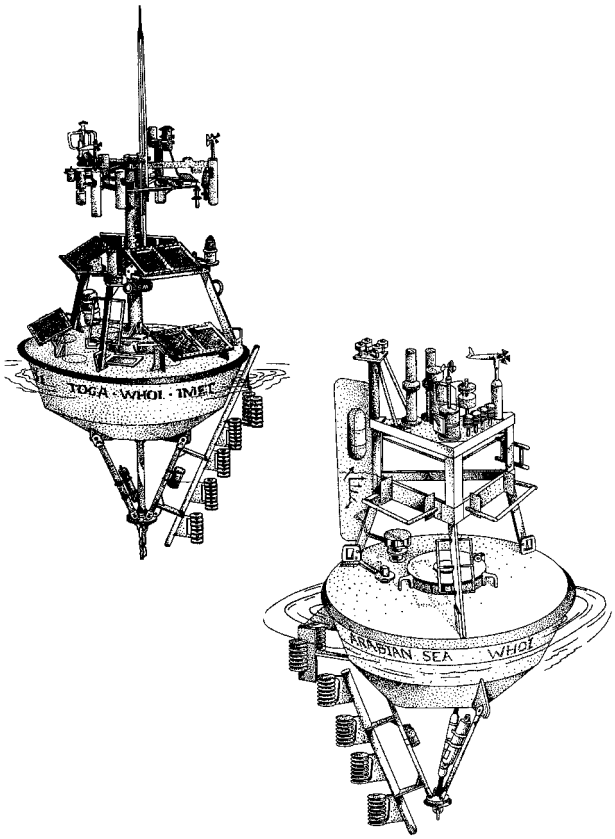


FIG. 2. Three-meter discus buoys used in the (a) TOGA COARE and (b) Arabian Sea Mixed Layer Dynamics experiments.

ble 1). The tropical Pacific measurements were part of TOGA COARE (for a full description, see Weller and Anderson 1996). This mooring was deployed at 156°E, 1.75°S from 21 October 1992 to 4 March 1993. This region is known for high sea surface temperatures (SST) and low wind speeds (typically $<3$ m $s^{-1}$), which are interrupted by infrequent but strong wind events ($>5$ m $s^{-1}$) associated with the intraseasonal oscillation (Weller and Anderson 1996) (Table 2). The Arabian Sea measurements were made off the coast of Oman at 15.5°N, 61.5°E during two back-to-back 6-month deployments spanning October 1993–October 1994 (for a full description, see Weller et al. 1997). This region is characterized by strong monsoonal winds, light intermonsoonal winds, small air–sea temperature differences, and typically clear skies (Table 2).

These buoys carried two independent meteorological instrument packages: the vector averaging wind recorder (VAWR) (Weller et al. 1990) and the improved meteorological (IMET) package (Hosom et al. 1995). The VAWR uses a thermistor element for measurement of air temperature, which is shielded by a 9-plate radiation shield based on the design by Gill (1983) (R. M. Young model 41002). The VAWR logs the mean temperature over the last 3.75 min of its 7.5-min sample period. The IMET air temperature module uses a platinum resistance thermometer (PRT) and is shielded by a 12-plate radiation shield. The IMET module discretely samples at 1 Hz and logs 1-min averages. These are the two primary air temperature measurements on the buoy. Additional air temperature observations are obtained from the IMET humidity module and a stand-alone humidity sensor (Way 1996). Both of these instruments have a thermistor collocated with the Rotronic MP 100 relative humidity sensor that is inside a porous Teflon cap surrounded by Gill multiplate radiation shields. All of these temperature elements have an accuracy of better than 0.01°C in the Woods Hole Oceanographic Institution calibration laboratory (Payne et al. 1976). The multiplate radiation shields are specified by R. M. Young, Inc., to yield root-mean-square air temperature errors under radiation intensity of 1080 W $m^{-2}$ of 0.4°, 0.7°, and 1.5°C at 3, 2, and 1 m $s^{-1}$, respectively.

In addition to the naturally ventilated air temperature modules, an IMET aspirated temperature module was deployed on the TOGA COARE buoy and on the two Arabian Sea buoys (Arab 1 and Arab 2). This module consists of an R. M. Young Aspirated Shield (Model 43408) with a dc motor-driven fan that has a power consumption of 0.5 A at 12 V and an aspiration rate of 3 m $s^{-1}$. This instrument is specified to have an error of no more than ±0.2°C under 1080 W $m^{-2}$ heating from solar radiation.

The TOGA COARE buoy used a symmetrical meteorological tower that consisted of a central mast with three arms (Fig. 2a). Two of the arms each supported a pair of IMET air temperature and humidity modules at

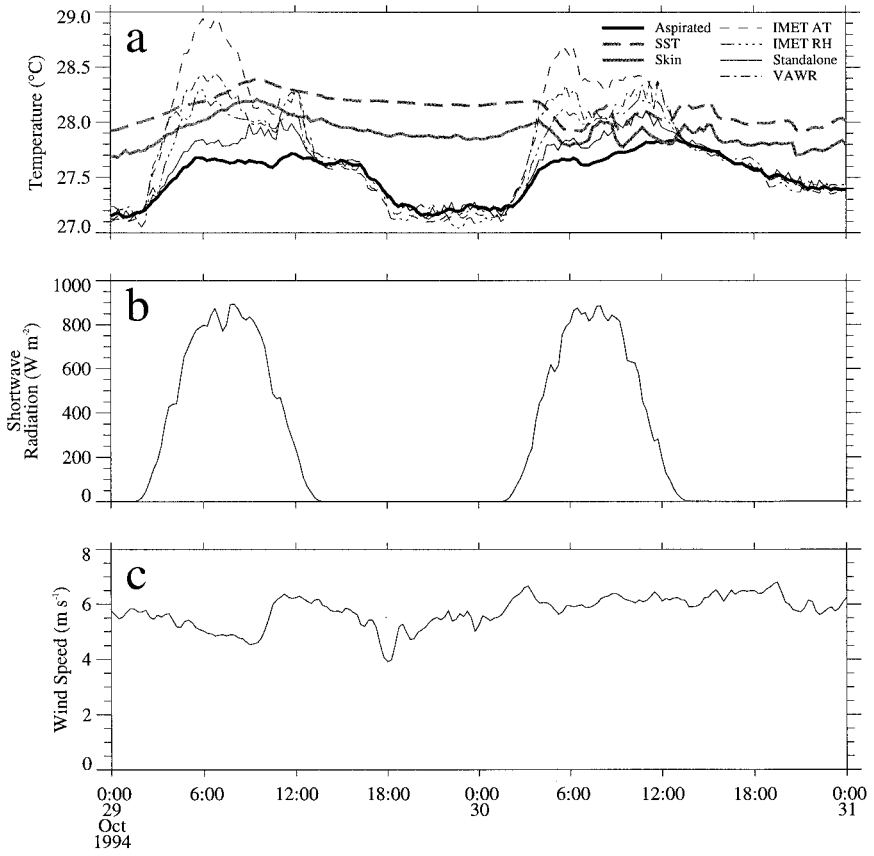


FIG. 3. Observations from 2-day time series during Arab 1 including (a) air temperatures from the aspirated, IMET, IMET RH, stand-alone, and VAWR sensors, sea surface temperature, and predicted cool-skin temperature [estimated using parameterization of Fairall et al. (1996b)], (b) shortwave radiation, and (c) wind speed.

a height of 2.6 m above the mean water line. The VAWR air temperature and humidity modules were inverted and attached to the third arm at a height of 2.7 m. An IMET aspirated air temperature and humidity module was located just beneath the supporting structure at a height of 2.6 m. This module drew power from batteries in the buoy well that were charged by solar panels. The aspiration was controlled by software that turned the aspirator off when the measured shortwave radiation fell below 200 W $m^{-2}$, thus saving energy (this control system was not used in future deployments in favor of continuous aspiration). No aspiration was used at night and a programming error turned off the aspirator for half an hour at 1200 LT. The aspiration system functioned for 13 days starting on 21 October 1992.

The Arabian Sea buoy used an asymmetrical tower with a large wind vane (Fig. 2b). The naturally ventilated IMET and VAWR air and humidity modules were located opposite the vane, on the upwind side of the buoy at a height of 2.7 m above the mean water line. In low winds, however, the buoy vane does not provide enough torque to rotate the buoy into the wind. A self-logging air temperature/humidity module (referred to hereafter as the stand-alone sensor) with a sample period of 3.75 min was placed near the center of the buoy at a height of 3.0 m. The IMET aspirated air temperature (with no collocated humidity) was located just beneath the supporting structure at a height of 2.2 m. A dedicated battery supply was connected to the aspirator providing enough power for continuous (day and night) operation for approximately 2 months. The first buoy (Arab 1) was deployed on 15 October 1994 and the aspirator ran for 59 days. The second buoy (Arab 2) was deployed on 22 April 1995 and the aspirator ran for 51 days.

The sensible and latent heat fluxes used in this study are estimated using aerodynamic bulk formulas (Fairall et al. 1996a). These formulas were tuned for estimating the net heat flux to within 10 W $m^{-2}$ in the Tropics during TOGA COARE. The flux algorithm is based on methods developed by Liu et al. (1979) with modifications for, but not limited to, low wind regimes. The sea surface skin or ''cool skin'' temperature (i.e., the temperature of the upper few millimeters of the ocean) used in these formulas was estimated using the parameterization of Fairall et al. (1996b). The specific humidity for the flux calculations was derived from the shielded, collocated relative humidity and air temperature sensors for the Arabian Sea data and from the

TABLE 3. Mean heating errors (°C) in naturally ventilated, shielded temperature measurements. Daytime and nighttime average biases from the reference aspirated temperature are reported as well as the standard deviation of the biases. Diurnal range is calculated from the mean diurnal cycle (Fig. 4).

| | Day | | Night | | Mean diurnal range |
|---|---|---|---|---|---|
| | Bias | Std dev | Bias | Std dev | |
| Arab 1 | | | | | |
| Stand-alone | 0.12 | 0.11 | 0.00 | 0.05 | 0.68 |
| IMET RH | 0.21 | 0.24 | 0.00 | 0.07 | 0.76 |
| VAWR | 0.33 | 0.27 | 0.00 | 0.05 | 0.89 |
| IMET AT | 0.34 | 0.40 | −0.01 | 0.06 | 0.96 |
| Arab 2 | | | | | |
| Stand-alone | 0.22 | 0.25 | 0.00 | 0.02 | 1.12 |
| IMET RH | 0.21 | 0.27 | 0.00 | 0.04 | 1.12 |
| VAWR | 0.29 | 0.35 | 0.01 | 0.04 | 1.15 |
| IMET AT | 0.17 | 0.33 | 0.01 | 0.03 | 1.03 |
| TOGA COARE | | | | | |
| IMET RH | 0.07 | 0.23 | — | — | — |
| VAWR | 0.90 | 0.66 | — | — | — |
| IMET AT | 0.12 | 0.27 | — | — | — |
| Mean | 0.27 | 0.31 | 0.00 | 0.04 | |

aspirated collocated pair for TOGA COARE. All flux calculations for the same deployment used identical input variables (e.g., wind speed, sea surface temperature, specific humidity, etc.) except for the different air temperature measurements. The errors in the sensible and latent heat fluxes due to radiative heating are reported relative to the reference heat flux (the flux estimated from the aspirated air temperature). We have chosen to use the oceanographic convention that positive heat fluxes are associated with ocean heating and atmospheric cooling.

## 3. Observations

A typical, 2-day time series of air temperature measured from each of the various sensors illustrates the radiative heating (Fig. 3). The data are from Arab 1 during a period of moderate, near constant winds and clear skies. The four naturally ventilated measurements agree well with the aspirated temperatures at night and have a mean nighttime bias of less then 0.01°C and standard deviation of less than 0.07°C (Table 3). Thus, the sensor elements themselves are well calibrated. It is during the day that the various temperature measurements are seen to diverge. The aspirated sensor reports the lowest daytime temperature, while the IMET air temperature reports the largest, reaching a maximum of 1.35°C above the aspirated temperature during this 2-day time period. The stand-alone unit performs the best of the naturally ventilated sensors. This unit is located higher and is more exposed to the wind than the other sensors. The mean and standard deviation of the differences between the aspirated and the naturally ventilated sensors are given in Table 3. Note that the TOGA COARE VAWR sensor has by far the largest daytime bias. The sensor element for this instrument was inverted in the multiplate shield for the experiment, which did not allow for adequate shielding and ventilation.

Also shown in Fig. 3 is the measured sea temperature at a depth of 0.89 m and the estimated surface skin temperature (Fairall et al. 1996b). The aspirated air temperature remains at or just below the skin temperature. These observations are consistent with an unstable or near neutral boundary layer. All of the naturally ventilated air temperatures are significantly above the skin temperature at some point during the 2-day period. At these times, the air–sea temperature differences and sensible heat fluxes calculated using naturally ventilated measurements are of the wrong sign, as can be seen in Fig. 4a. The instantaneous sensible heat flux estimates from the naturally ventilated sensors have a maximum error of 22.5 W $m^{-2}$ during the three deployment periods. Changes in the latent heat flux estimates only reflect changes in the calculated boundary layer stability from changes in the air–sea temperature difference since the air–sea humidity difference is not varied (Fig. 4b). The mean latent heat flux values are much larger than the sensible heat fluxes, but the daytime mean errors are nearly the same size (Tables 4 and 5). These daytime biases contribute to a 0.5–8.6 W $m^{-2}$ reduction in mean daytime ocean cooling induced by the estimated latent and sensible heat fluxes.

The mean diurnal cycles (Fig. 5) and diurnal ranges (Table 3) from the naturally ventilated measurements also show clear evidence of radiative heating errors. The radiative heating leads to mean diurnal range errors that are nearly as large as the true diurnal temperature range. The difference between the air and sea surface temperatures is small enough on average during Arab 1 that the mean daytime air temperature from the naturally ventilated sensors is larger than the skin temperature. Besides the bias, the shape of the mean diurnal cycle is also significantly altered by radiative heating. In Arab 1, there is a broad maximum aspirated temperature located between 1200 and 1500 LT, while several of the naturally ventilated sensors report a midmorning maximum and decrease through the afternoon. In Arab 2, the aspirated temperature has a distinct maximum in the late afternoon (1700 LT), while all the naturally ventilated sensors report double peaks occurring in midmorning and late afternoon.

Part of this shape change in the diurnal cycle is associated with the sensitivity of the solar heating to shield geometry and solar elevation. Gill (1983) reports ''maximum heating occurred in all shields with a sun [elevation] of 40° to 70°. (This was not expected, but seems to be of no great significance.)'' However, this sensitivity has a direct effect on the errors in diurnal cycles from naturally ventilated air temperature sensors. Consider the case of Arab 1 and 2 deployments whose mean diurnal cycles are given in Fig. 5. The Arab 2 measurements were made in May at 15.5°N when the sun

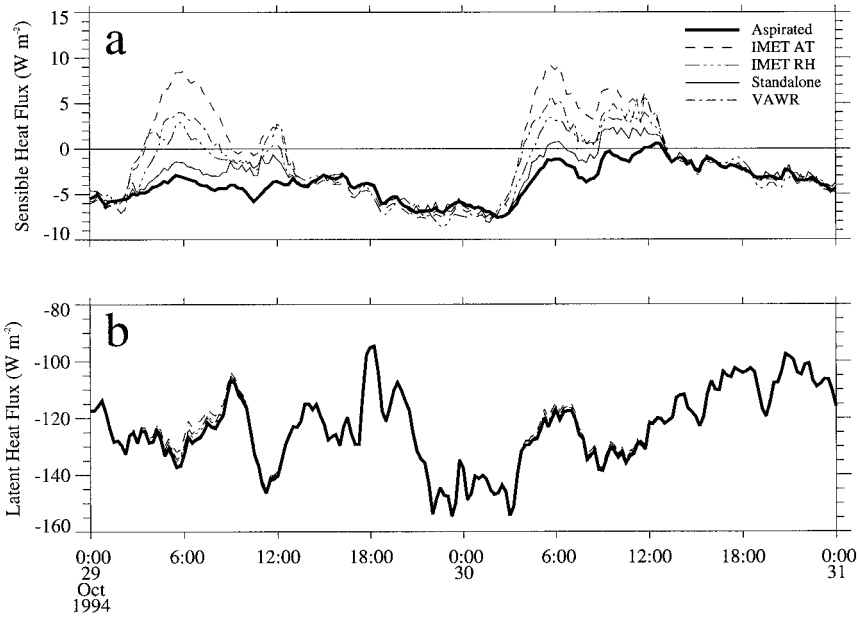


FIG. 4. (a) Sensible and (b) latent heat fluxes computed from each of the air temperature sensors for the same sample 2-day time series depicted in Fig. 2.

was passing nearly directly overhead at 1200 LT each day during the observing period. All nonaspirated Arab 2 air temperatures have clear midmorning and late afternoon peaks relative to the aspirated temperature (Fig. 6). If the sample period is during a time of year when the sun is passing directly overhead each day, the radiative heating errors are reduced at 1200 LT relative to midmorning and midafternoon as Gill suggests. This double peaked signal is not as obvious in the Arab 1 data, which were taken in November when the sun elevation never reached above 66°. A more subtle double peak is most evident in the stand-alone temperature since it was located high enough on the buoy to minimize variability due to wind blocking or solar shading by other instruments. Thus, contrary to Gill's (1983)

TABLE 4. Mean errors in sensible heat flux (W m$^{-2}$). Average daytime biases from the reference sensible heat flux (computed from the aspirated temperature) are reported as well as the standard deviation of the biases. All fluxes were calculated using bulk formulas (Fairall et al. 1996a). Sensible heat fluxes computed from the raw and corrected air temperatures are reported.

| | Raw | | | | | |
|---|---|---|---|---|---|---|
| | Day | | Night | | Corrected day | |
| | Bias | Std dev | Bias | Std dev | Bias | Std dev |
| Arab 1 | | | | | | |
| Stand-alone | 1.2 | 1.0 | 0.0 | 0.9 | −0.2 | 1.0 |
| IMET RH | 1.9 | 1.7 | 0.0 | 1.4 | −0.2 | 1.2 |
| VAWR | 3.0 | 2.1 | 0.0 | 0.8 | −0.2 | 1.7 |
| IMET AT | 2.9 | 3.1 | 0.0 | 1.2 | −0.3 | 1.5 |
| Arab 2 | | | | | | |
| Stand-alone | 1.2 | 0.8 | 0.0 | 0.2 | 0.2 | 0.8 |
| IMET RH | 1.2 | 1.1 | 0.0 | 0.3 | −0.1 | 1.0 |
| VAWR | 1.6 | 1.2 | 0.1 | 0.2 | −0.2 | 1.2 |
| IMET AT | 0.7 | 1.2 | 0.1 | 0.2 | 0.0 | 1.0 |
| TOGA COARE | | | | | | |
| IMET RH | 0.2 | 1.2 | — | — | −0.4 | 1.0 |
| VAWR | 5.3 | 3.9 | — | — | −0.5 | 3.3 |
| IMET AT | 0.4 | 1.4 | — | — | −0.5 | 1.3 |
| Mean | 1.8 | 1.7 | 0.0 | 0.6 | −0.2 | 1.4 |

TABLE 5. Mean errors in latent heat flux (W m$^{-2}$). Average daytime biases from the reference latent heat flux (computed from the aspirated temperature) are reported as well as the standard deviation of the biases. All fluxes were calculated using bulk formulas (Fairall et al. 1996a) and specific humidity calculated from collocated relative humidity and air temperature measurements. Latent heat fluxes computed from the raw and corrected air temperatures are reported.

| | Raw | | | | | |
|---|---|---|---|---|---|---|
| | Day | | Night | | Corrected day | |
| | Bias | Std dev | Bias | Std dev | Bias | Std dev |
| Arab 1 | | | | | | |
| Stand-alone | 0.5 | 0.5 | 0.0 | 0.1 | −0.2 | 0.5 |
| IMET RH | 0.9 | 1.2 | 0.0 | 0.2 | −0.1 | 0.6 |
| VAWR | 1.4 | 1.5 | 0.0 | 0.1 | −0.1 | 0.8 |
| IMET AT | 1.4 | 2.0 | 0.0 | 0.2 | −0.1 | 0.7 |
| Arab 2 | | | | | | |
| Stand-alone | 0.8 | 1.0 | 0.0 | 0.1 | 0.2 | 0.7 |
| IMET RH | 0.8 | 1.3 | 0.0 | 0.1 | −0.1 | 0.7 |
| VAWR | 1.1 | 1.7 | 0.0 | 0.1 | −0.1 | 1.0 |
| IMET AT | 0.7 | 1.6 | 0.0 | 0.1 | 0.1 | 1.1 |
| TOGA COARE | | | | | | |
| IMET RH | 0.3 | 0.9 | — | — | −0.1 | 0.6 |
| VAWR | 3.3 | 3.0 | — | — | −0.1 | 1.5 |
| IMET AT | 0.4 | 1.0 | — | — | −0.2 | 0.7 |
| Mean | 1.0 | 1.4 | 0.0 | 0.1 | −0.1 | 0.8 |

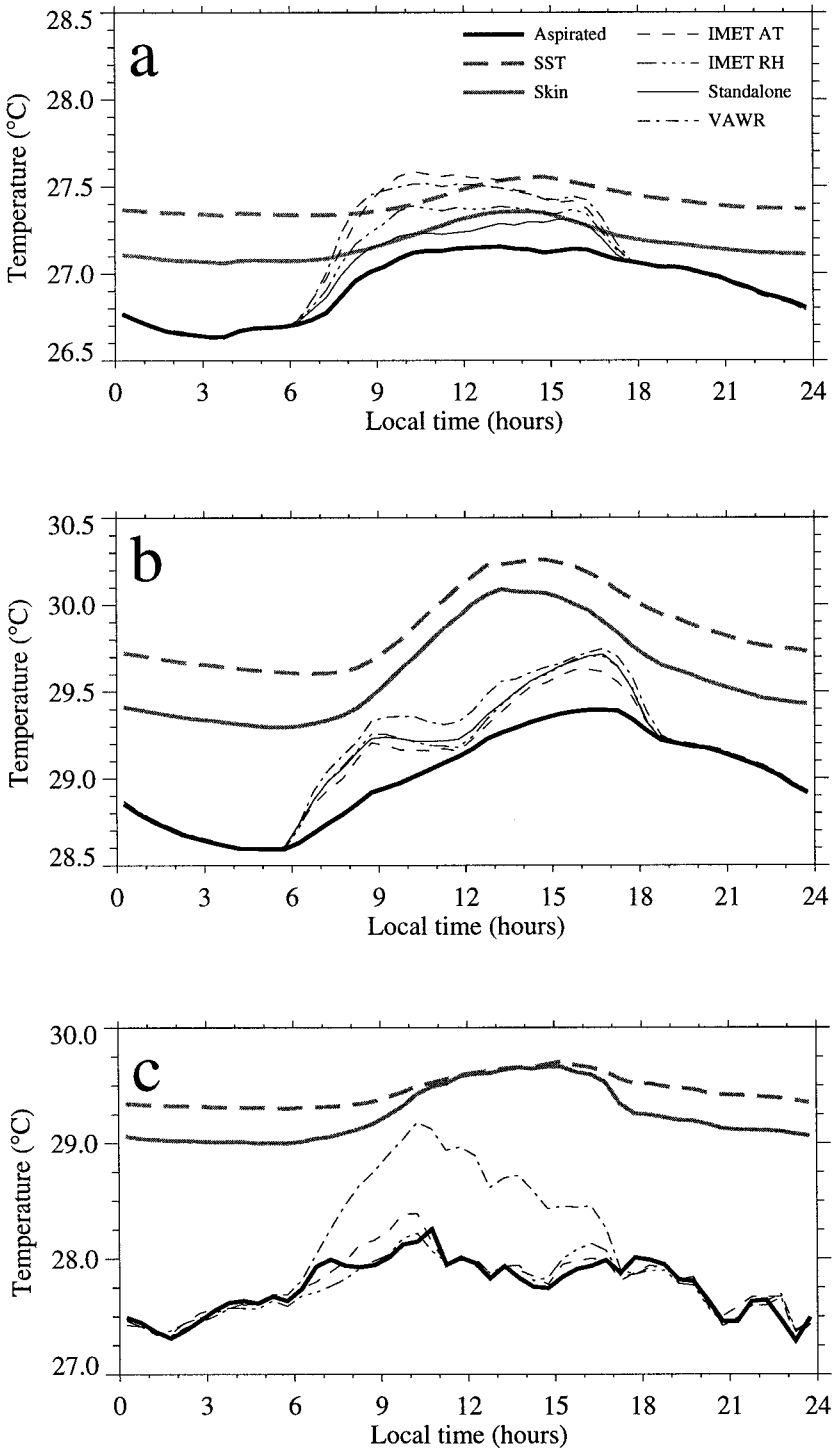


FIG. 5. Mean diurnal cycles in air temperature and sea surface temperature for (a) Arab 1, (b) Arab 2, and (c) TOGA COARE.

statement, the sensitivity of radiative heating to sun elevation is of great significance to those studying the diurnal cycle of the atmospheric boundary layer. This issue is explored further in the model described in the next section.

Relative humidity sensor elements are also often placed in naturally ventilating radiation shields. Theoretically, if the air around a sensor element heats up relative to the ambient air, the relative humidity will change but the specific humidity will remain constant.

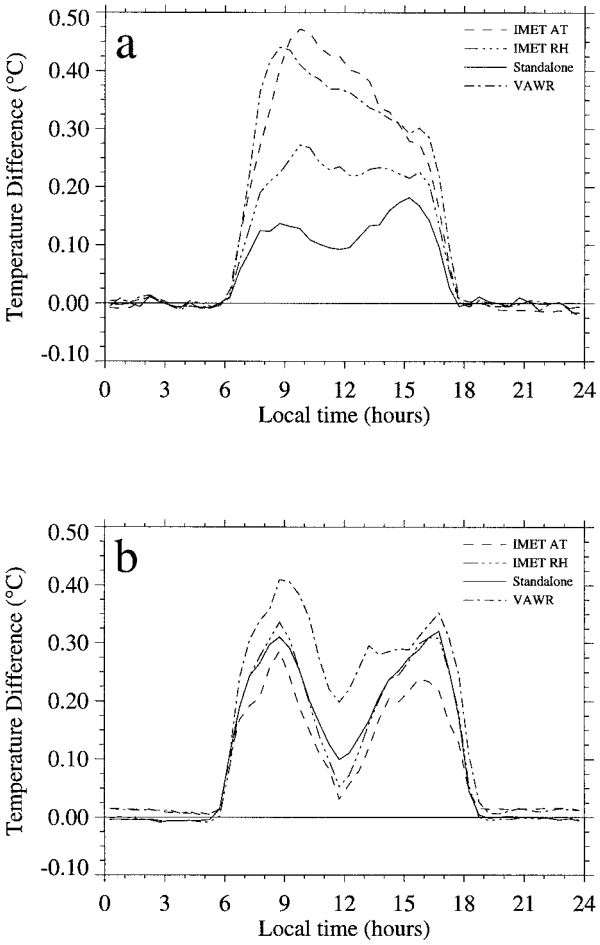


FIG. 6. Mean diurnal cycles of the shielded air temperatures relative to the aspirated temperature during (a) Arab 1 and (b) Arab 2. Note the pronounced double peak in the Arab 2 diurnal cycles compared with the more subtle double peak in Arab 1, especially in the standalone sensor.

Thus, if the temperature of the air at the relative humidity sensor is known, then the specific humidity estimates should not be significantly affected by radiative heating. Collocated air temperature and relative humidity sensors were deployed during each of the experiments. Specific humidities calculated from collocated shielded and collocated aspirated air temperature and relative humidity sensors were compared to determine the effect of radiative heating on humidity measurements and hence, latent heat fluxes. Despite radiative heating errors in the shielded air temperature measurements, collocated shielded and collocated aspirated specific humidities agreed well. At 0500 UTC 25 October 1992 during TOGA COARE (Fig. 7), the naturally ventilated air temperature is higher and the relative humidity is lower than the corresponding measurements from the aspirated sensor pair due to radiative heating. However, the specific humidity from each sensor pair remains in agreement. These observations indicate that collocation of air temperature and relative humidity sensors can minimize radiative heating errors in derived specific humidities. If the specific humidity is conserved and the ambient air temperature is measured accurately, a simple calculation will yield the ambient relative humidity. Note that the apparent offset of 0.2 g kg$^{-1}$ in the specific humidity time series in Fig. 7 is within the $\pm$0.2 g kg$^{-1}$ measurement accuracy for specific humidity found in dedicated ship-buoy intercomparisons during TOGA COARE [Weller and Anderson (1996); also see Kent and Taylor (1996) for a description of radiative heating effects on humidity measurements made from ships].

## 4. Model of radiative heating

### *a. Heat budget*

The heat balance on the radiation shield surface sufficient for this study is

$$\alpha_s R_s A_s + \alpha_t R_t A_t = \varepsilon_t \sigma T^4 A_t + L + S, \qquad (1)$$

where $R_s$ and $R_t$ are the flux densities of solar and thermal radiation incident to the shield surface, $\alpha_s$ and $\alpha_t$ are the solar and thermal absorptivities, $\varepsilon$ is the thermal emissivity, $A_s$ and $A_t$ are the areas normal to the incident solar and thermal radiation, and $L$ and $S$ are the convective and conductive heat losses. The blackbody emission of the shield surface is $\sigma T^4$ where $\sigma$ is the Stefan–Boltzmann constant and $T$ is the shield's surface temperature in degrees kelvin. Assuming the shield is a graybody, the thermal emissivity is equal to the thermal absorptivity. The solar radiative heat flux is the dominate heating term during daylight hours. This is balanced largely by convective cooling with a lesser proportion of cooling from conductive and thermal radiative cooling. The response time of the temperature module to changes in air temperature and surface heating is assumed to be much shorter than averaging interval for measurements. Thus, at any given time, the temperature of the module is assumed to be in steady-state heat balance.

### *b. Radiative heating*

Fuchs and Tanner (1965) examine the limit of nonconvective heat loss where the heat balance of a radiation shield surface is between the radiation components (this situation is found in the vacuum of space). They show that choosing a shield coating that minimizes the ratio of $\alpha_s$ to $\alpha_t$ will minimize the temperature of the shield surface. However, this is an extreme limit. In the laboratory studies of Gill (1983) for the case of constant radiative heating, the shielded temperatures are a clear function of forced convection even at wind speeds down to 0.5 m s$^{-1}$. It is likely that even with no forced convection, the free convective cooling will be larger than the thermal radiative cooling of the shield. If this were not the case, then under nighttime, low wind, clear sky conditions, the shielded temperature modules would

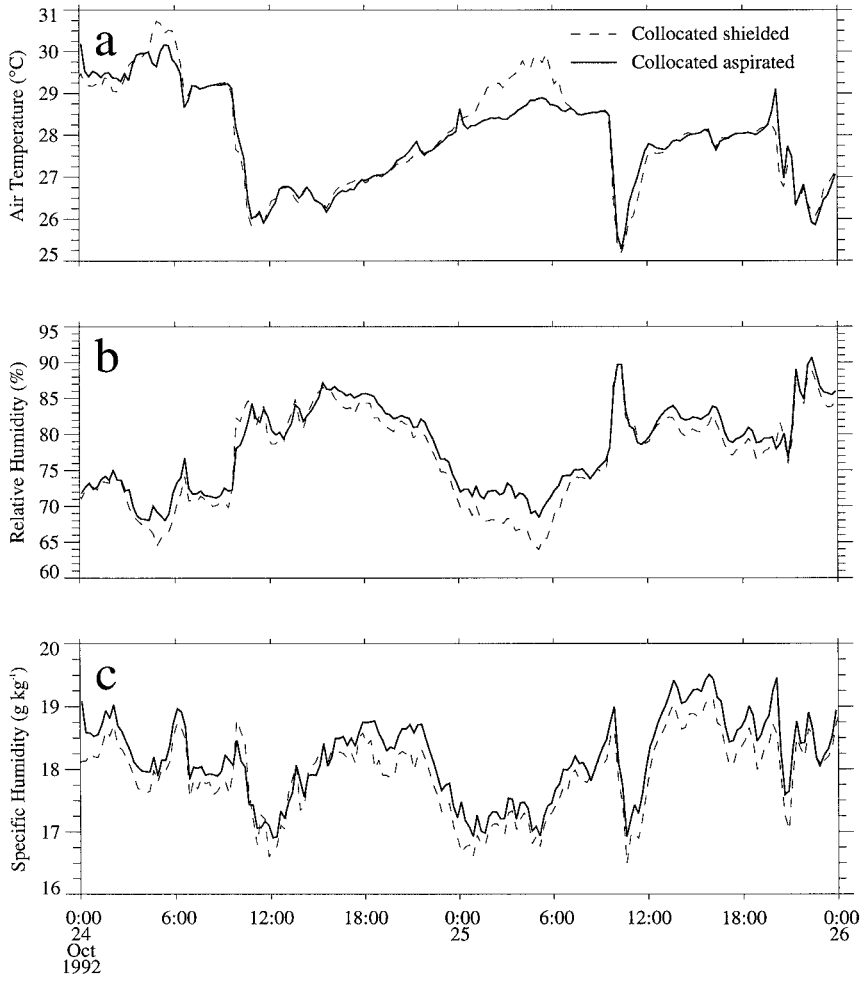


FIG. 7. Comparison of specific humidities computed from relative humidity and air temperature measurements collected with the collocated, naturally ventilated sensors and collocated, aspirated sensors during the TOGA COARE experiment. Comparisons of (a) air temperature, (b) relative humidity, and (c) specific humidity are shown.

cool from thermal radiation heat loss to the upper atmosphere, and the temperature elements would be measurably lower than the aspirated temperatures. This is not seen in these observations. Thus, it is assumed that the thermal radiation balance can be neglected in these calculations.

The heat flux due to the solar radiation is proportional to the absorptivity of the shield, the flux density of the radiation, and the area of exposure that is normal to the ray path. The shortwave flux density $R_s$ is calculated using the measured shortwave radiation normal to the ocean surface and the calculated sun elevation (List 1984). No measurement is made to separate the diffuse from the direct solar radiation. Under clear sky conditions, most of the solar radiation is direct, but under cloudy skies the proportion of diffuse radiation is much larger. Here, we assume a constant ratio of clear to total radiation of 0.9. The justification is that the largest radiative heating occurs under clear skies rather than cloudy. Under cloudy conditions, the ratio of clear to total radiation is significantly different, but the radiative heating errors are small due to reduced insolation. At these times, the choice of the clear to total radiation ratio is less important. The area of the shield normal to the solar radiation flux path is a function of sun elevation. For this calculation, it is assumed that the shield is cylindrical in shape with height $h$ and radius $r$. The solar radiation term of the heat budget is written as

$$\alpha_s R_s A_s = \alpha_s \frac{\mathrm{SW}\downarrow}{(0.1 + 0.9 \sin\theta)}[r\pi(\mathrm{h}\cos\theta + r\sin\theta)], \tag{2}$$

where $\theta$ is the sun elevation and SW$\downarrow$ is the flux density of shortwave radiation normal to the sea surface. A single Gill radiation plate has a radius of 6 cm and a height of 1.5 cm. Typical shield configurations have 9–12 plates.

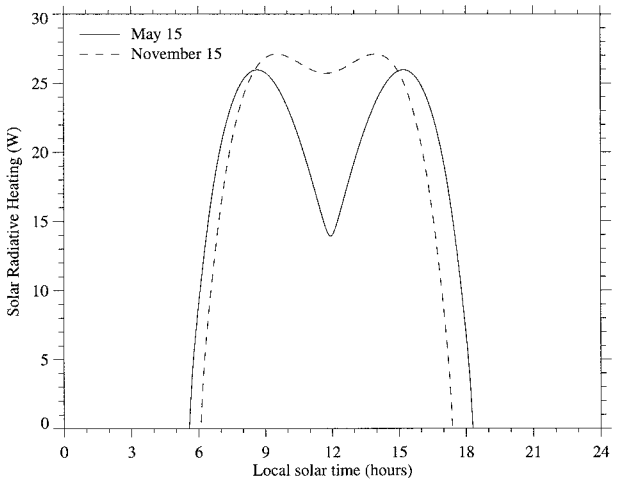


FIG. 8. Radiative heating ($R_S A_S$) of a 9-plate radiation shield at 15.5°N on 15 November (Arab 1) and 15 May (Arab 2). Radiative heating is computed from the theoretical clear sky radiation (SW↓), solar elevation angle ($\theta$), and the shield geometry ($r$, $h$) from Eq. (2) in the text.

With this geometry, there is more surface area exposed to solar radiation at low sun angles than at high sun angles. Thus, the solar radiative heating is larger at the lower sun angles. This heating is slightly reduced, though, since solar radiation flux density decreases at lower sun angles because the radiation must travel through a larger portion of the atmosphere prior to reaching the surface. Under clear sky conditions, the solar radiative heating for a 9-plate shield will be largest for a sun elevation of 42°. This sensitivity to sun angle is consistent with Gill's (1983) laboratory investigations. The solar radiative heating of a 9-plate shield is computed as a function of time of day by calculating the theoretical clear sky solar radiation and sun elevation for 15 November (Arab 1) and 15 May (Arab 2) at 15.5°N (Fig. 8). A double peak is evident in the estimated solar radiative heating for May, but a much less pronounced double peak is found in November since the maximum sun elevation is not much above the critical heating angle of 42° at this time of year. This is consistent with the Arab 1 and 2 observations, whose mean error in the diurnal cycles are given in Fig. 6.

### c. Convective and conductive cooling

The convective and conductive heating terms are both proportional to the temperature difference between the shield surface and the ambient air, and proportional to the surface area. The temperature of the shield surface is assumed to be equal to that of the temperature element inside the shield. Thus, the cooling terms are written as

$$L + S = h_u(T - T_a)A_c + h_o(T - T_a)A_c, \quad (3)$$

where $T$ is the shield surface temperature, $T_a$ is the ambient air temperature, $A_c$ is the surface area, and $h_u$ and $h_o$ are the heat transfer coefficients for forced convective and conductive cooling, respectively. For simplification, the shape of the multiplate radiation shield is assumed to be cylindrical and $A_c$ is equal to $2\pi r(h + r)$. The conductive cooling coefficient is a constant, but the convective cooling coefficient is a function of wind speed. Both coefficients must be determined empirically.

Empirical models of forced convective cooling coefficients involving simple geometrically shaped objects usually begin with a nondimensionalization resulting in a balance among the Nusselt (Nu, ratio of convective and conductive thermal diffusivities); Reynolds (Re, ratio of inertial and viscous forces); and Prandtl (Pr, ratio of the momentum and thermal diffusivities) numbers. In cases of flow over a cylinder, the average convective cooling coefficient $h_u$ is as follows (Incropera and DeWitt 1985):

$$\mathrm{Nu} = C'\mathrm{Re}^m\mathrm{Pr}^n \quad (4)$$

$$\frac{h_u D}{\kappa} = C'\left(\frac{VD}{\upsilon}\right)^m \mathrm{Pr}^n, \quad (5)$$

where $D$ is the diameter of the cylinder, $\kappa$ is the thermal conductivity of the cylinder, $\upsilon$ is the viscosity, $V$ is the wind speed, and $C'$, $m$, and $n$ are empirically determined constants. Here, Pr, $\upsilon$, and $\kappa$ are taken as constant over the air temperatures typically observed. The expression for the average convective cooling coefficient then reduces to the form

$$h_u = CV^m, \quad (6)$$

where $C$ is a constant. Combining (1), (3), and (6) and dividing by $\alpha_s$, the estimated sum of the convective and conductive cooling coefficients (hereafter referred to as the cooling function), $\delta$, is

$$\delta = (CV^m + h_o) = \frac{R_s A_s}{(T - T_a)A_c}, \quad (7)$$

where the constants $C$ and $h_o$ are normalized by the solar absorptivity. While the aspirator is in operation on the buoy, $T_a$ is the aspirated temperature and $T$ is the shielded temperature, and all of the variables in (2) and (7) are available. The three empirical constants, $C$, $m$, and $h_o$, are determined from the concurrent aspirated and shielded temperature observations. The correction for radiative heating then becomes

$$T_c = T - \frac{R_S A_S}{\delta A_C}, \quad (8)$$

where $T$ is the observed shielded temperature and $T_c$ is the corrected temperature.

To estimate the empirical constants, all $\delta$ are computed from the available 15-min averaged data using the right-hand side of (7). These data are then classified by wind speed using equal sample/probability class sizes (Kendall and Stuart 1967). This approach is used to

TABLE 6. Summary of the empirically derived constants, $C$ (J m$^{-3}$ °C$^{-1}$), $m$ (nondimensional), and $h_o$ (W m$^{-2}$ °C$^{-1}$), from the radiative heating model for each sensor during the Arabian Sea and TOGA COARE experiments.

| Sensor | Experiment | $C$ | $m$ | $h_o$ |
|---|---|---|---|---|
| IMET | Arab 1 | 62.51 | 1.61 | 187.05 |
| | Arab 2 | 107.56 | 1.84 | 337.74 |
| | TOGA COARE | 42.13 | 1.69 | 236.79 |
| IMET RH | Arab 1 | 103.90 | 1.54 | 192.04 |
| | Arab 2 | 109.60 | 1.36 | 118.51 |
| | TOGA COARE | 276.02 | 1.04 | 276.43 |
| VAWR | Arab 1 | 45.97 | 1.18 | 193.02 |
| | Arab 2 | 34.08 | 1.51 | 163.26 |
| | TOGA COARE | 81.42 | 1.03 | 147.00 |
| Stand-alone | Arab 1 | 43.21 | 1.75 | 1039.30 |
| | Arab 2 | 28.74 | 1.98 | 1033.23 |

minimize the influence of classes that have very few observations. The constant $h_o$ is estimated as 99% of the median $\delta$ in the lowest wind class. A nonlinear least squares regression is performed to obtain $C$ and $m$ by using the median value of $\delta$ in each class as the ordinate and the average wind speed in each class as the abscissa in the regression. The constants derived for each sensor in the field experiments, after applying the wind blocking and sun shading adjustments described in section 4d, are reported in Table 6.

### *d. Wind blocking and sun shading adjustments*

Other instruments on the buoy tower can shade the radiation shield from the sun or block it from the wind depending on the orientation of the buoy with respect to the sun and wind (Fig. 2). When corrected temperatures from (8) do not agree well with the aspirated temperatures, sun shading or wind blocking is suspected. Corrected air temperatures are expected to be higher than the aspirated temperatures during times of wind blocking and lower than the aspirated temperatures during times of sun shading. The effects of wind blocking are assumed to be a function of the wind direction relative to the buoy, although a full description of the wind flow around the buoy tower would require extensive wind tunnel testing. An evaluation of the wind flow field is beyond the scope of this study. While sun shading is clearly a function of both the sun's elevation and azimuth, only the azimuthal angle is used to develop a correction.

Wind blocking reduces the wind speed experienced by the shield and thereby decreases the rate of convective cooling. By assuming that the difference between the observed wind speed and the wind speed at the shield is proportional to the difference between the aspirated and corrected shielded temperatures for a given wind direction relative to the buoy, the wind speed at the shield can be estimated. This proportion is determined empirically from the observations by first classifying the difference between the aspirated and corrected temperatures by wind direction relative to the buoy using equal sample/probability class sizes (Kendall and Stuart 1967). A lookup table of temperature differences by wind direction is created from the average wind direction relative to the buoy and the median temperature difference in each class. The temperature differences in the lookup table are then converted to a wind blocking percentage function of the form

$$B(\psi) = 1 - \frac{D(\psi) - D_{\min}}{D_{\max} - D_{\min}}, \tag{9}$$

where $B(\psi)$ is the blocking percentage ranging from 0 to 1, $\psi$ is the wind direction relative to the buoy, $D(\psi)$ is the temperature difference in the lookup table associated with $\psi$, and $D_{\min}$ and $D_{\max}$ are the minimum and maximum temperature differences in the lookup table, respectively. Both the lookup table and wind blocking function for the Arab 1 shielded IMET air temperature sensor are shown in Fig. 9 to illustrate the conversion in (9). The angle $\psi$ equals 0° when the buoy vane points downwind and the sensors face into the wind. The smallest temperature differences for a given wind speed and radiative heating are observed near $\psi = 0°$, corresponding to no wind blocking, while the largest temperature differences are seen near $\psi = 90°$ when the cases and shields from the other instruments block the wind and reduce ventilation. The blocking function is applied to the observed wind speed $V$ to estimate the wind speed at the shield $\hat{V}$ as

$$\hat{V} = B(\psi)V. \tag{10}$$

The estimated wind speed at the shield is used in (7)

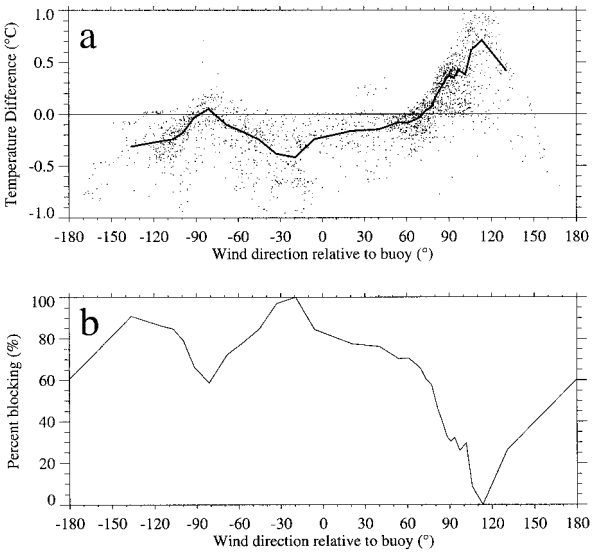


FIG. 9. Wind blocking function for the IMET air temperature sensor during Arab 1. (a) The lookup table of temperature differences by wind direction relative to the buoy (dark line) is shown over all observations (dots). (b) The wind blocking percentage function $B(\psi)$, computed from the lookup table in (a) using Eq. (9) where $\psi$ is the wind direction relative to the buoy.

to derive a new set of empirical constants and in (8) to correct the original shielded temperatures.

A correction for sun shading is determined in a similar manner to the correction for wind blocking. Sun shading reduces the amount of solar radiation incident on the shield and thereby decreases the rate of radiative heating. Again, the correction seeks to estimate the actual solar radiation experienced by the shield by reducing the observed solar radiation by an amount proportional to the temperature difference between the aspirated and the corrected shielded temperatures after applying the wind blocking correction. After classifying the temperature differences by the sun's azimuthal angle relative to the buoy, a lookup table of average azimuthal angles and median temperature differences is created. The lookup table is transformed to a sun shading function yielding

$$S(\phi) = \frac{D(\phi) - D_{\min}}{D_{\max} - D_{\min}}, \tag{11}$$

where $S(\phi)$ is the shading percentage ranging from 0 to 1, $\phi$ is the sun's azimuthal angle relative to the buoy, $D(\phi)$ is the temperature difference in the lookup table associated with $\phi$, and $D_{\min}$ and $D_{\max}$ are the minimum and maximum temperature differences in the lookup table, respectively. This shading function is applied to the solar radiation to estimate the actual solar radiation incident on the shield $\hat{R}_s$, such that

$$\hat{R}_s = S(\phi)R_s. \tag{12}$$

The estimated solar radiation at the shield is used in (7) to derive a new set of empirical constants and the final correction is

$$T_c = T - \frac{\hat{R}_S A_S}{\delta A_C}, \tag{13}$$

where

$$\hat{\delta} = (C\hat{V}^m + h_o). \tag{14}$$

The empirical constants for each sensor in Arab 1, Arab 2, and TOGA COARE were determined using the radiative heating and convective cooling model described above after wind blocking and sun shading corrections were applied (Table 6). The exception is the stand-alone sensor that has no correction for wind blocking and sun shading. The estimated cooling functions computed from $C$, $m$, and $h_o$ for each sensor are provided in Fig. 10. Variation in the constants from one sensor to another and from one deployment to another is in part due to the different mounting and shield arrangements. The stand-alone sensor has a much larger $h_o$ than the other sensors, which reflects the increased ventilation of this sensor at low wind speed. The coefficient $m$ varies from 1.0 to 2.0, thus doubling the wind speed alone will reduce heating errors by 50%–75%.

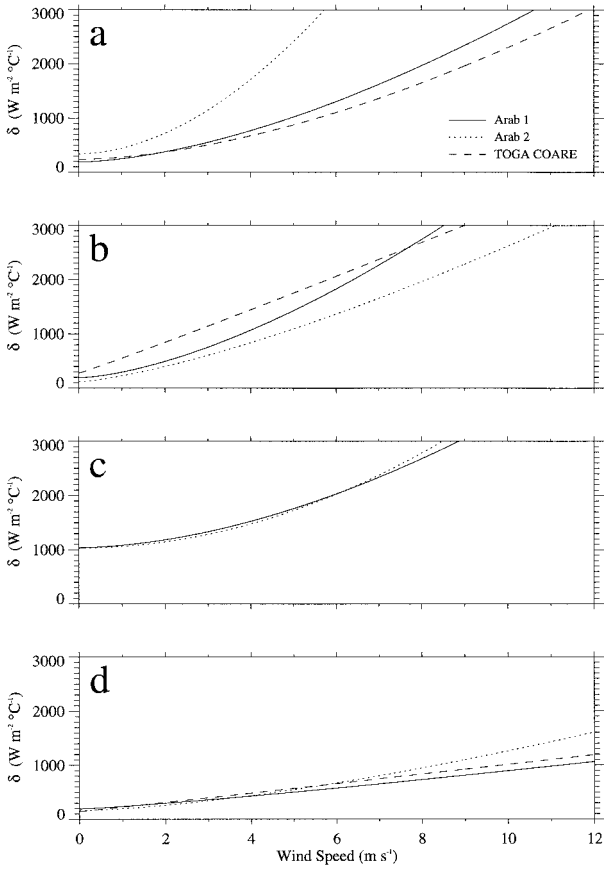


FIG. 10. Cooling functions vs wind speed for (a) IMET, (b) IMET RH, (c) stand-alone, and (d) VAWR air temperature sensors for Arab 1 (solid), Arab 2 (dotted), and TOGA COARE (dashed).

## 5. Model results

The effectiveness of the model was evaluated in two analyses. The first is a comparison of the aspirated time series with the air temperatures that have been corrected using model constants derived from the same aspirated time series. This is presented only to demonstrate the model's ability to capture the effects of radiative heating, wind blocking, and sun shading in the same dataset from which the empirical coefficients were derived. The second analysis is a more rigorous evaluation of the model that applies a set of average constants obtained in the first analysis to each of the temperature time series. This analysis tests how well the model performs with constants determined independently of the data.

The same 2-day time series in Fig. 3 is shown again in Fig. 11 with the adjusted air temperatures. During this time period, all of the adjusted temperatures now are within 0.4°C of the aspirated temperature and do not rise significantly above the surface skin temperature. As a further illustration of the model, consider the 16-day record of corrected and raw temperatures from the IMET shielded air temperature sensor deployed in Arab 1 (Fig. 12). During this period, the wind speed varies

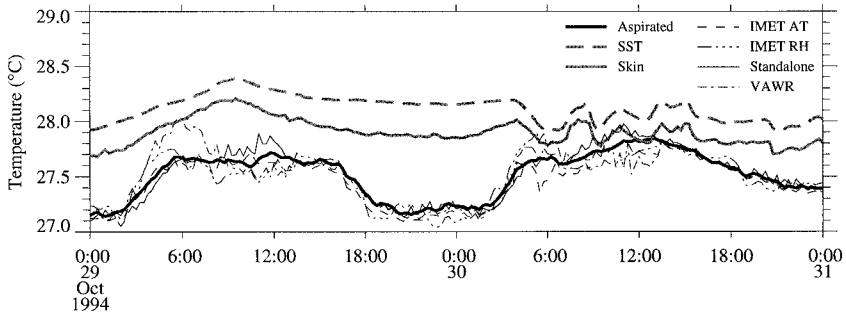


FIG. 11. Corrected air temperatures for the same sample 2-day time series depicted in Fig. 2.

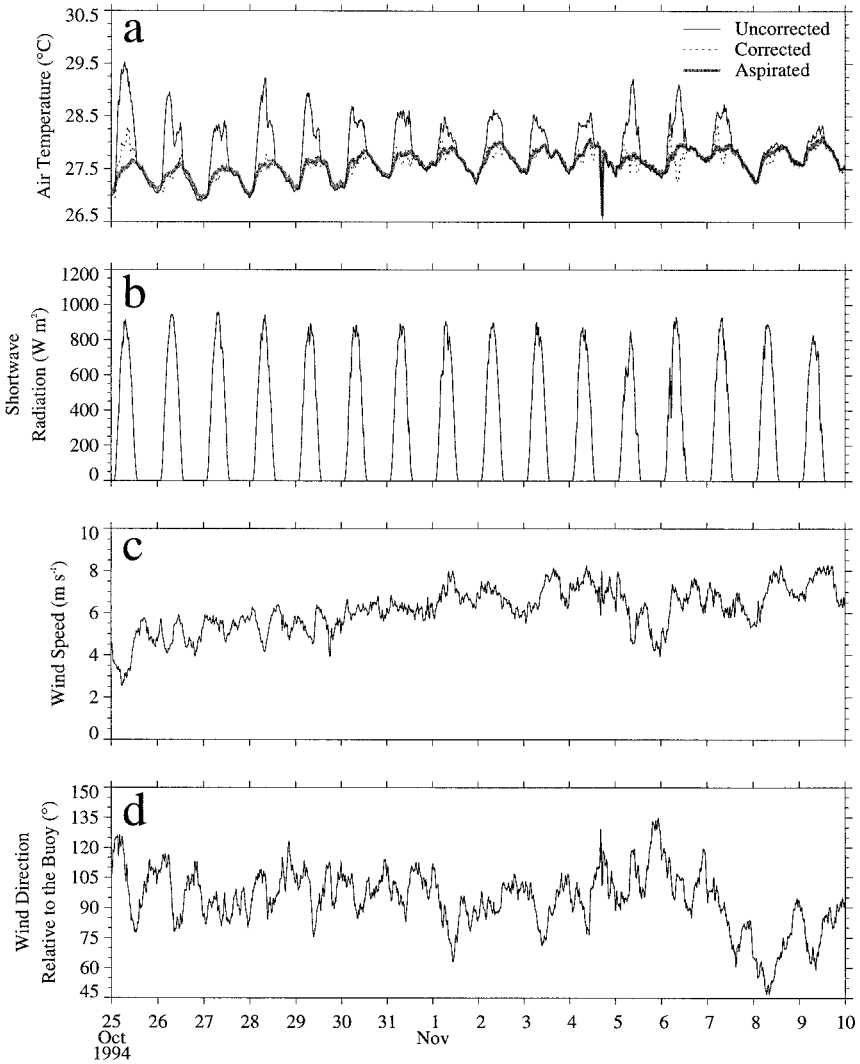


FIG. 12. Example of corrected and raw air temperatures. A 16-day time period from Arab 1 shows the (a) raw, corrected, and aspirated temperatures, (b) shortwave radiation, (c) wind speed, and (d) wind direction relative to the buoy. The raw and corrected IMET shielded air temperatures are shown.

TABLE 7. Mean daytime heating errors (°C) in corrected air temperatures. Average daytime biases from the reference aspirated temperature are reported as well as the standard deviation of the biases. Air temperatures have been corrected using the algorithm described in the text. Diurnal range is calculated from the mean diurnal cycle.

| | Day | | Mean diurnal range |
|---|---|---|---|
| | Bias | Std dev | |
| Arab 1 | | | |
| Stand-alone | −0.03 | 0.11 | 0.54 |
| IMET RH | −0.02 | 0.14 | 0.50 |
| VAWR | −0.02 | 0.19 | 0.53 |
| IMET AT | −0.02 | 0.18 | 0.50 |
| Arab 2 | | | |
| Stand-alone | 0.07 | 0.22 | 0.97 |
| IMET RH | −0.03 | 0.18 | 0.88 |
| VAWR | −0.02 | 0.26 | 0.87 |
| IMET AT | 0.02 | 0.25 | 0.87 |
| TOGA COARE | | | |
| IMET RH | −0.05 | 0.16 | — |
| VAWR | −0.01 | 0.44 | — |
| IMET AT | −0.06 | 0.19 | — |
| Mean | −0.02 | 0.21 | |

from 2.5 to 8.2 m $s^{-1}$ and the shortwave from clear sky to partly cloudy. The wind direction relative to the buoy varies from 45° to 135°. The largest radiative heating error (1.8°C) corresponds to the period of lowest wind speed, and the temperature correction has reduced this maximum error to 0.55°C. Near zero radiative heating error is found during 8–9 November when high winds impact the sensor side of the buoy. Some radiative heating is observed during 3–4 November, which have similar winds speeds and shortwave as 8–9 November but with winds impacting on the side and rear of the buoy. During these varied forcing conditions, the algorithm successfully removes the radiative heating errors without overcorrecting, although some minor discrepancies still can be found between the corrected and the aspirated temperatures. In general, daytime biases are significantly decreased from an average bias of 0.27°C for all naturally ventilated sensors before applying the radiative heat corrections (Table 3) to −0.02°C after the corrections (Table 7). In addition to lowering the mean daytime bias and standard deviation, the mean diurnal ranges are much closer to the aspirated diurnal ranges (Table 2).

As before, both the sensible and latent heat fluxes for the corrected temperatures are computed using bulk formulas. All flux calculations for the same deployment use identical input variables except for air temperature (Tables 4 and 5). The daytime biases in sensible heat flux are significantly reduced from an average 1.8 W $m^{-2}$ for all sensors to an average of −0.2 W $m^{-2}$ after the air temperature corrections are applied. The daytime biases in latent heat flux are also reduced from an average of 1.0 to −0.1 W $m^{-2}$ after corrections are applied. While the reductions in the sensible and latent heat flux biases are of approximately the same magnitude, the correction to the sensible heat flux is most dramatic due to the relatively small magnitude of the sensible heat flux. The average bias in sensible heat flux during Arab 1 was 2.25 W $m^{-2}$; however, the average sensible heat flux is only −2.0 W $m^{-2}$, making the average error in sensible heat flux due to radiative heating errors 113% of the mean sensible heat flux. Conversely, the average error in latent heat flux due to radiative heating during Arab 1 is only 0.7%. This is illustrated in the original and corrected sensible and latent heat fluxes during the 2-day time series of 29–30 October 1994 (Figs. 4 and 13).

The improvements in latent heat flux are due only to changes in the boundary layer stability caused by correcting air temperatures for radiative heating. The major source of error in the latent heat flux, however, is not due to radiative heating, but the performance of the humidity sensor. During dedicated ship–buoy intercomparisons in TOGA COARE, the accuracy of the specific humidity computed from naturally ventilated, collocated air temperature and relative humidity measurements was estimated to be ±0.2 g $kg^{-1}$ (Weller and Anderson 1996). By applying a constant bias of 0.2 and −0.2 g $kg^{-1}$ to the Arabian Sea specific humidity values and recomputing the heat fluxes, the accuracy of the latent heat flux due to bulk measurement errors was estimated to be approximately ±5 W $m^{-2}$. The error in latent heat flux due to radiative heating can therefore be considered significant, ranging between 6% and 66% of the error caused by uncertainties in measuring specific humidity. To work toward the goal of estimating the net heat flux within ±10 W $m^{-2}$ as set forth in TOGA COARE, the errors in latent heat flux due to radiative heating should not be ignored.

To assess the performance of the model more rigorously, an independent estimate of the model constants was used to adjust air temperatures from similar sensors (the IMET, VAWR, and collocated IMET air temperature and relative humidity sensors) during both Arabian Sea deployments. The average of the constants from five of the sensors (Table 6) was used as the independent estimate to adjust the sixth sensor's measurements. For example, the air temperature from the collocated air temperature and relative humidity sensor (IMET RH) deployed during Arab 1 was adjusted using a set of averaged constants from the Arab 1 IMET and VAWR and the Arab 2 IMET, IMET RH, and VAWR air temperatures. This set of average constants can be considered independent since the air temperature of interest was not used to derive the model constants. The results of comparing each sensor's adjusted air temperatures to the aspirated time series are presented in Table 8. In each case, wind blocking and sun shading corrections were omitted and only the model [Eq. (8)] was applied using the reported average model constants. In four of the six cases, the absolute mean daytime bias in air temperature is reduced by over 50%. The Arab 2 adjusted IMET and IMET RH time series have large neg-

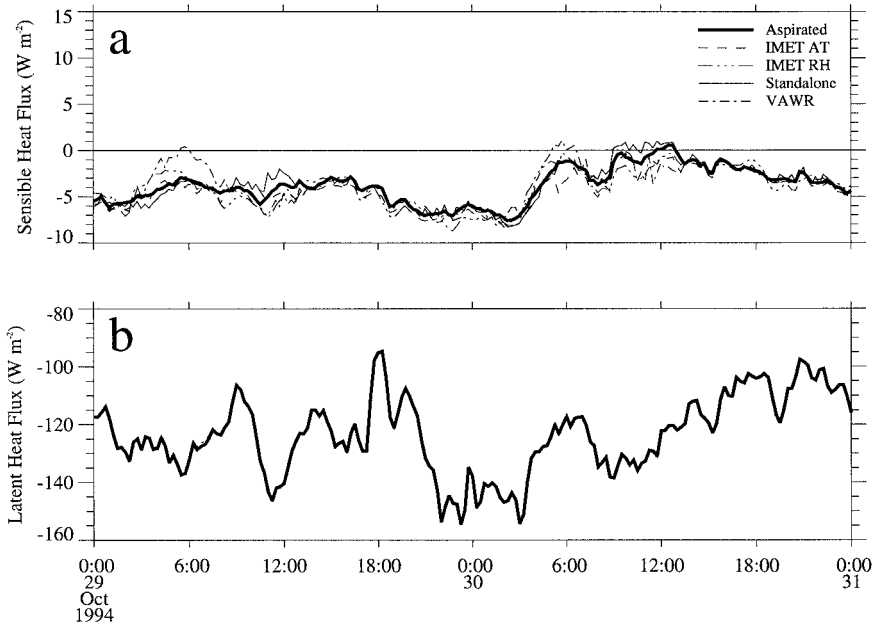


FIG. 13. (a) Sensible and (b) latent heat fluxes computed from each of the air temperature sensors corrected for radiative heating for the same sample 2-day time series depicted in Fig. 2.

ative biases, indicating that the model is overcorrecting to produce air temperatures that are cooler than the aspirated temperature. In the case of the IMET air temperature, this is due to the underestimation of the cooling function $\delta$ from the average model coefficients and hence an overestimation of the required adjustment [Eq. (8)].

## 6. Conclusions

Instantaneous errors in naturally ventilated air temperature measurements made from buoys due to radiative heating as large as 3.4°C are observed during conditions of low wind and high solar insolation. Radiative heating errors likely occur in most buoy air temperature measurements, not just the observations presented here. For example, consider the TOGA TAO buoys in the Pacific Ocean that use naturally ventilated air temperature sensors (Hayes et al. 1991). These buoys are located near the equator where the daily maximum sun elevation is always above 67°. Monthly averaged mean diurnal cycles computed from four TAO buoys (Fig. 14) located on the equator demonstrate the similar double peak signal as the Arabian Sea observations (Fig. 5b). This is suggestive of radiative heating errors, as are the early morning air–sea temperature inversions seen in the mean diurnal cycles. In addition to buoy measurements, Kent et al. (1993) show that even shipboard naturally ventilated sensors may not be adequately ventilated during transit to prevent radiative heating errors.

The radiative heating model described here can be used to correct daytime air temperature measurements for radiative heating errors. The application of the model requires simultaneous measurements of shortwave radiation, wind speed and direction, and aspirated air temperature to determine the model constants for a particular buoy tower arrangement and sensor design. After the model constants have been determined, only shortwave radiation and wind speed and direction are necessary. Provided the shielded temperature sensor is located well away from other instruments or structures so that there is no wind blocking or sun shading, only shortwave radiation and wind speed are necessary.

The preferred solution for eliminating radiative heating errors in air temperature measurements is to employ a fan aspirator. While this is feasible on coastal or shipboard platforms with unlimited power supplies, long duration buoy deployments have very narrow power constraints. Development of a low-power aspirator is

TABLE 8. Mean and standard deviation of daytime heating errors (°C) in air temperatures corrected using average model coefficients, $C$ (J m$^{-3}$ °C$^{-1}$), $m$ (nondimensional), and $h_o$ (W m$^{-2}$ °C$^{-1}$). The mean diurnal range of the corrected air temperatures (°C) is also provided.

| | | | | Day | | Mean diurnal |
|---|---|---|---|---|---|---|
| | $C$ | $m$ | $h_o$ | Bias | Std dev | range |
| Arab 1 | | | | | | |
| IMET RH | 71.94 | 1.50 | 199.91 | −0.05 | 0.21 | 0.51 |
| VAWR | 83.53 | 1.57 | 199.72 | 0.12 | 0.23 | 0.65 |
| IMET AT | 80.22 | 1.49 | 200.91 | 0.09 | 0.36 | 0.67 |
| Arab 2 | | | | | | |
| IMET RH | 70.80 | 1.54 | 214.62 | −0.14 | 0.22 | 0.82 |
| VAWR | 85.91 | 1.51 | 205.67 | −0.05 | 0.22 | 0.88 |
| IMET AT | 71.21 | 1.44 | 170.77 | −0.24 | 0.28 | 0.73 |

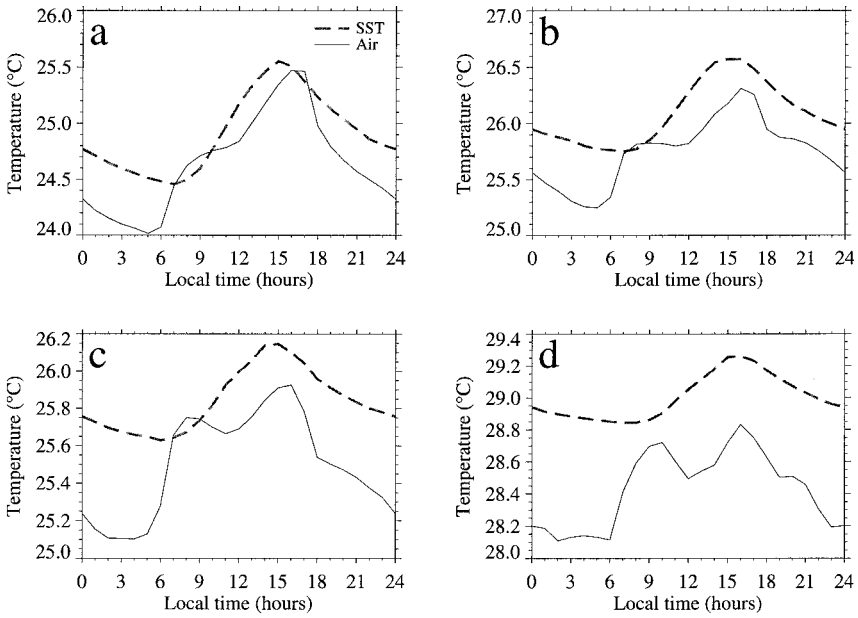


FIG. 14. Mean diurnal cycles of air and sea surface temperature measured from four TOGA TAO buoys at various locations along the equator. Mean diurnal cycle is computed over 30 days of observations centered on (a) 23 March 1995 at 110°W, (b) 23 March 1994 at 125°W, (c) 23 June 1992 at 140°W, and (d) 23 June 1994 at 180°W.

required to support the measurement of more accurate air temperatures from buoys.

*Acknowledgments*. Our participation in TOGA COARE was supported by the National Science Foundation, Grant OCE91-10559. Participation in the Arabian Sea Project was supported by the Office of Naval Research, Grant N00014-94-1-0161. We thank Dr. R. A. Weller for his forethought to include the aspirator on the TOGA COARE and Arabian Sea IMET buoys and providing the data. Dr. R. E. Payne and Dr. Weller participated in useful discussions regarding the results of our findings. Assistance from all members of the WHOI Upper Ocean Processes Group during all phases of the work and during the preparation of this manuscript is gratefully acknowledged.

## REFERENCES

Esbensen, S. K., and M. J. McPhaden, 1996: Enhancement of tropical ocean evaporation and sensible heat flux by atmospheric mesoscale systems. *J. Climate,* **9,** 2307–2325.

Fairall, C. W., E. F. Bradley, D. P. Rogers, J. B. Edson, and G. S. Young, 1996a: The parameterization of air–sea fluxes for Tropical Ocean-Global Atmosphere Coupled-Ocean Atmosphere Response Experiment. *J. Geophys. Res.,* **101,** 3734–3764.

——, ——, J. S. Godfrey, G. A. Wick, J. B. Edson, and G. S. Young, 1996b: The cool skin and the warm layer in bulk flux calculations. *J. Geophys. Res.,* **101,** 1295–1308.

Fuchs, M., and C. B. Tanner, 1965: Radiation shields for air temperature thermometers. *J. Appl. Meteor.,* **4,** 544–547.

Gill, G. C., 1983: Comparison testing of selected naturally ventilated solar radiation shields. NOAA Data Buoy Office Rep., Bay St. Louis, MS, in partial fulfillment of Contract NA-82-0A-A-266, 38 pp. [Available from NOAA/National Data Buoy Center, Bay St. Louis, MS 39529.]

Hayes, S. P., L. J. Mangum, J. Picaut, A. Sumi, and K. Takeuchi, 1991: TOGA-TAO: A moored array for real-time measurements in the tropical Pacific Ocean. *Bull. Amer. Meteor. Soc.,* **72,** 339–347.

Hosom, D. S., R. A. Weller, R. E. Payne, and K. E. Prada, 1995: The IMET (Improved Meteorology) ship and buoy system. *J. Atmos. Oceanic Technol.,* **12,** 527–540.

Incropera, F. P., and D. P. DeWitt, 1985: *Fundamentals of Heat Transfer*. John Wiley and Sons, 802 pp.

Kendall, M. G., and A. Stuart, 1967: *The Advanced Theory of Statistics*. Vol. 2. Griffon and Co. Limited, 690 pp.

Kent, E. C., and P. K. Taylor, 1996: Accuracy of humidity measurement on ships: Consideration of solar radiation effects. *J. Atmos. Oceanic Technol.,* **13,** 1317–1321.

——, R. Tiddy, and P. Taylor, 1993: Correction of marine air temperature observations for solar radiation effects. *J. Atmos. Oceanic Technol.,* **10,** 900–906.

Lin, X., and R. H. Johnson, 1996: Heating, moistening, and rainfall over the western Pacific warm pool during TOGA COARE. *J. Atmos. Sci.,* **53,** 3367–3383.

List, R. J., 1984: *Smithsonian Meteorological Tables*. Smithsonian Institution Press, 527 pp.

Liu, W. T., K. B. Katsaros, and J. A. Businger, 1979: Bulk parameterization of the air–sea exchange of heat and water vapor including the molecular constraints at the interface. *J. Atmos. Sci.,* **36,** 1722–1735.

Payne, R. E., A. L. Bradshaw, J. P. Dean, and K. E. Schleicher, 1976: Accuracy of temperature measurements with the VACM. Tech. Rep. WHOI-76-94, 78 pp. [Available from Woods Hole Oceanographic Institution, Woods Hole, MA 02543.]

Way, B. S., 1996: A stand-alone relative humidity and air temperature logger. Woods Hole Oceanographic Institution Upper Ocean Processes Group January 1996 Tech. Note, 2 pp. [Available from Upper Ocean Processes Group, c/o Rick Trask, Woods Hole

Oceanographic Institution, Woods Hole, MA 02543. Also available at http://uop.whoi.edu]

Webster, P. J., and R. Lukas, 1992: TOGA COARE: The Coupled Ocean–Atmosphere Response Experiment. *Bull. Amer. Meteor. Soc.,* **73,** 1377–1416.

Weller, R. A., and S. P. Anderson, 1996: Temporal variability and mean values of the surface meteorology and air–sea fluxes in the western equatorial Pacific warm pool during TOGA COARE. *J. Climate,* **9,** 1959–1990.

——, D. L. Rudnick, R. E. Payne, J. P. Dean, N. J. Pennington, and R. P. Trask, 1990: Measuring near-surface meteorology over the ocean from an array of surface moorings in the subtropical convergence zone, *J. Atmos. Oceanic Technol.,* **7,** 85–103.